

Work Function Describes the Electrocatalytic Activity of Graphite for Vanadium Oxidation

Hannes Radinger,* Vanessa Trouillet, Felix Bauer, and Frieder Scheiba

Cite This: *ACS Catal.* 2022, 12, 6007–6015

Read Online

ACCESS |



Metrics & More



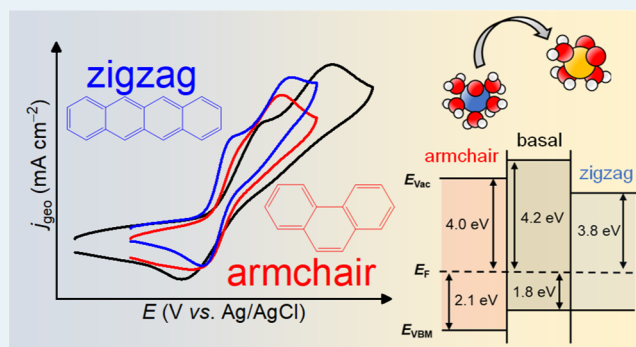
Article Recommendations



Supporting Information

ABSTRACT: In many applications such as vanadium flow batteries, graphite acts as an electrocatalyst and its surface structure therefore determines the efficiency of energy conversion. Due to the heterogeneity of the material, activity descriptors cannot always be evaluated with certainty because the introduction of defects is accompanied by a change in surface chemistry. Moreover, surface defects occur in multiple dimensions, and their occurrence and influence on catalysis must be separated. In this work, we have studied the surface of graphite felt electrodes by different methods in terms of morphology and chemistry to understand the electrocatalytic activity. We then defined the interaction between the surface and the electronic structure with particular emphasis on the work function and valence band. Using model catalysts with different architectures, we established correlations between the electrocatalytic activity and the size of the conjugation and the orientation of the edges. Finally, it was possible to link the level of the work function to the electrocatalytic activity.

KEYWORDS: graphite electrode, vanadium redox reaction, electronic structure, work function, edge sites, surface defects, photoelectron spectroscopy, activity descriptor



1. INTRODUCTION

Carbonaceous electrodes are becoming increasingly popular for electrochemical energy storage and conversion devices such as batteries, supercapacitors, and fuel cells.^{1–3} In graphitic materials, the surface structure determines the electrocatalytic properties and thus the efficiency of conversion from electrical to chemical energy and vice versa. Surface defects such as edge sites have been shown to provide faster kinetics for redox reactions in general and for vanadium redox reactions in particular.^{4–7} The reactivity of the less reactive basal layer can be adjusted by thermal or chemical treatments.^{8,9} The consequences of these activations are studied by spectroscopic or microscopic techniques to draw conclusions about the interplay between physicochemical properties and electrochemical activity. Due to the complicated interactions between morphology, surface chemistry, or microstructure, conclusions in the literature diverge, making it difficult to find common activity descriptors.¹⁰ Especially, with respect to the multitude of dimensions and geometries, the electrocatalytic role of various graphite defects should be explored. Complexity increases as one moves from model systems to heterogeneous, three-dimensional electrodes. However, a thorough understanding of these materials is necessary to advance the development of systems that rely on their use. An illustrative example is the graphite felt (GF) in vanadium flow batteries

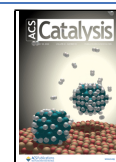
(VFBs). The integration of surface defects such as edge sites has been shown to be a reliable way to improve its activity toward the vanadium redox couples.^{5,11,12} Chemical stability and electrical conductivity of the material are preserved, while ions in the electrolyte find reaction sites with lower adsorption barriers.^{13,14} However, these edges occur in zigzag and armchair configurations, which must be understood in terms of their electrocatalytic activity in order to benefit from their different physical and chemical properties.

The importance of the structural properties for electrochemical processes shall be illustrated by describing the interface between graphite and the vanadium-containing electrolyte (Figure 1). At the surface of an immersed electrode, the so-called electrochemical double-layer forms.¹⁵ While the energy of the Fermi level (E_F) would theoretically match the equilibrium redox state of the solution, the arrangement of molecules in the double layer creates a potential barrier, which must be overcome for successful charge transfer. The total

Received: January 19, 2022

Revised: February 21, 2022

Published: May 12, 2022



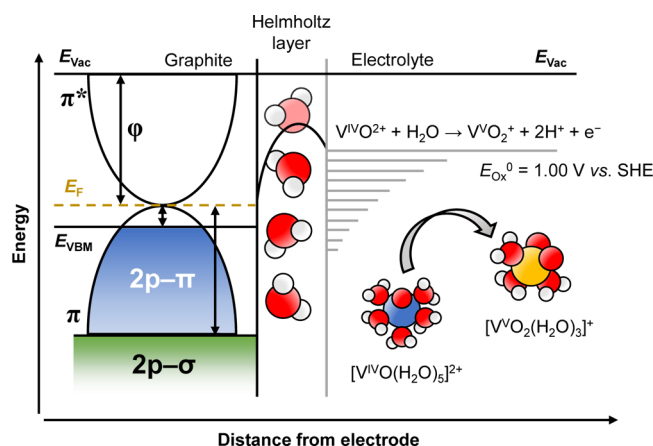


Figure 1. Schematic depiction of the graphite–electrolyte interface.

number of electron donor or acceptor levels of the electrolyte which are accessible to graphite (horizontal gray lines in Figure 1) could thus be increased by shifting the valence band maximum (VBM) upward, which is for instance achieved by doping.^{16–18} A different strategy seems appropriate as well: If the vacuum energy (E_{Vac}) is defined as zero, a lower work

function ($WF, \varphi = E_{\text{Vac}} - E_{\text{F}}$) brings E_{F} closer to the redox potential of the electrolyte. This was proven to be possible for metals such as copper to improve its charge transfer properties for electrocatalytic CO_2 reduction.¹⁹ However, experimental results on the influence of the WF vary and therefore cannot be readily extrapolated from one system to another. One study for Au–Ag alloys suggests more efficient CO_2 reduction by increasing the WF, while another work claims the opposite for silver electrodes.^{20,21} For nitrogen-doped carbon electrodes used in the oxygen reduction reaction, a lower WF has been found to be beneficial.²² Similarly, an increased WF of carbon due to surface oxidation was associated with the deactivation of Fe–N–C catalysts.²³ Using graphite, the edge orientation (zigzag or armchair) plays an important role for its catalytic and electronic properties.^{24,25} However, the relationship between activity, electronic structure, and morphology of graphite is far from sufficiently understood to define common activity descriptors.

Herein, we investigated a pristine and activated GF for the $\text{V}^{\text{VO}}\text{O}_2^+/\text{V}^{\text{IV}}\text{O}_2^+$ redox reaction to elaborate the correlation between electrocatalytic activity, physicochemical properties, and the electronic structure by combining results from half-cell electrochemistry, scanning electron microscopy (SEM), X-ray and UV photoelectron spectroscopy (XPS and UPS), as well as

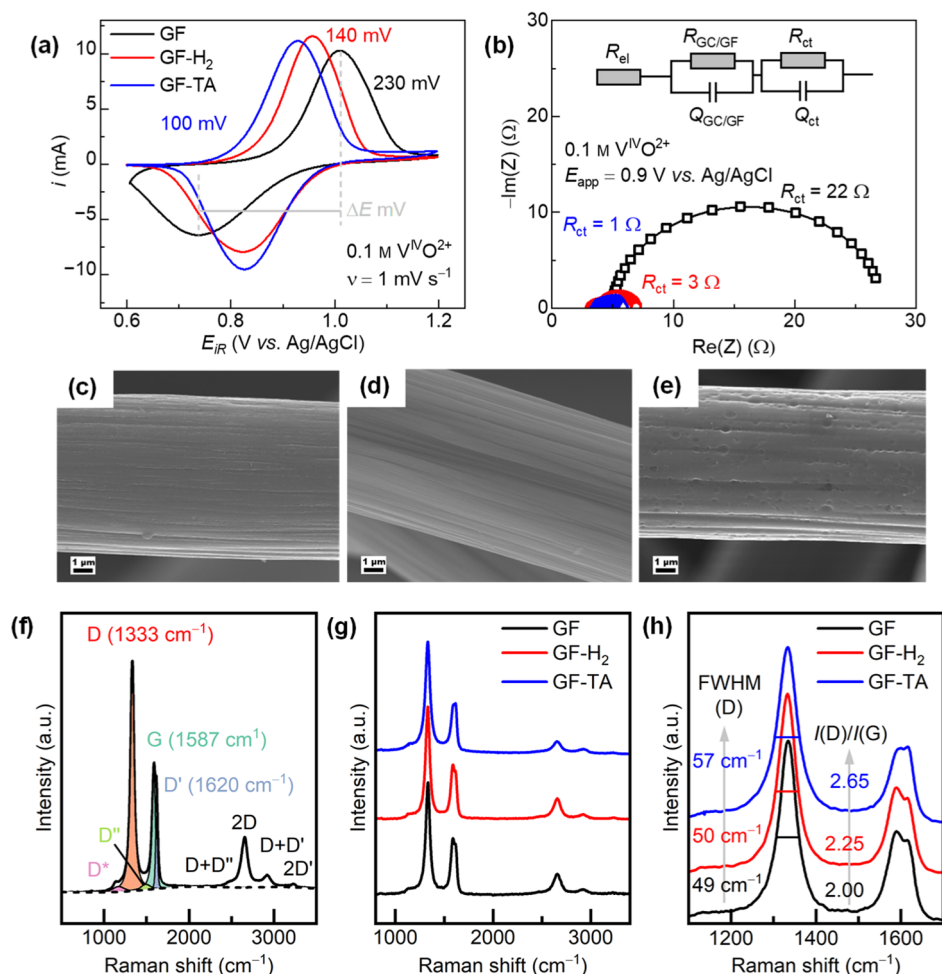


Figure 2. Electrochemical and structural characterization of GF. (a) CV in the positive half-cell, displaying ΔE between the $\text{V}^{\text{VO}}\text{O}_2^+/\text{V}^{\text{IV}}\text{O}_2^+$ redox peaks. (b) EIS at an applied potential to assess R_{CT} . (c–e) High-magnification SEM images showing the morphology of (c) GF, (d) GF- H_2 , and (e) GF-TA. (f–h) Raman spectra, illustrating (f) an exemplary deconvolution of the characteristic vibrational features of the GF; (g) each felt stacked for comparison, and (h) results of the deconvolution.

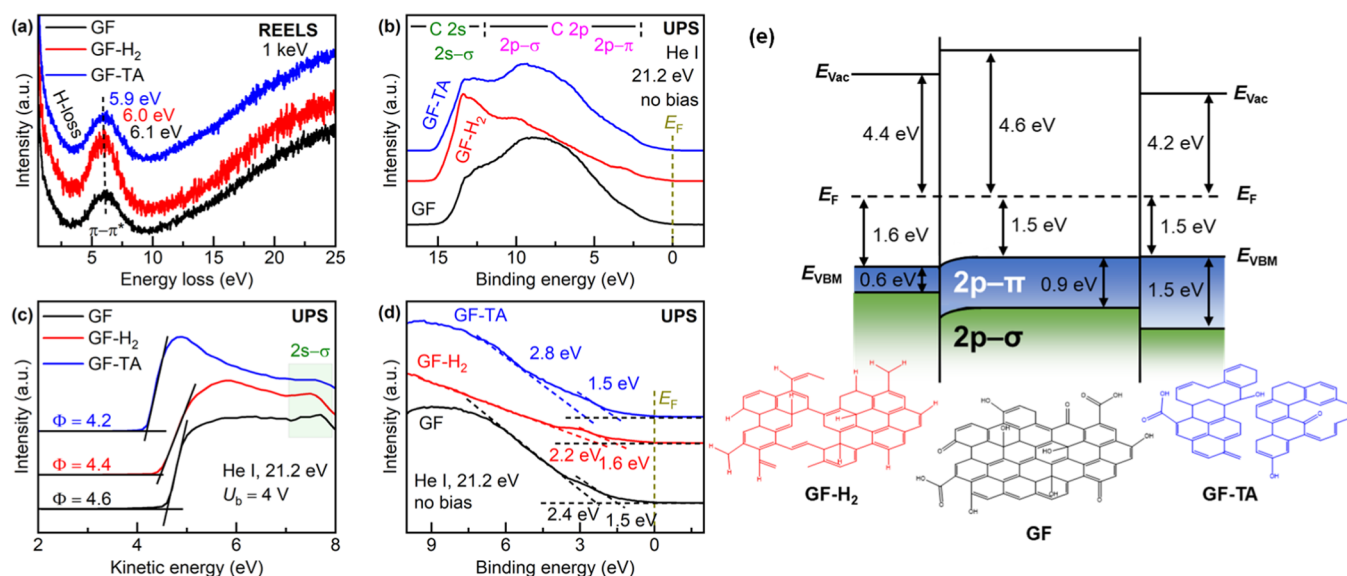


Figure 3. Electronic structure of the GF. (a) Integrity of the π -conjugated system analyzed by the π - π^* transition using REELS; (b) electronic density of states below E_F probed by UPS. (c) At an applied external bias, the cutoff energy of the valence electrons yields the WF. (d) Detailed investigation of the threshold energies close to E_F to determine the VBM. (e) By combining the information retrieved from UPS, an electronic band diagram is constructed.

Raman and reflection electron energy loss spectroscopy (REELS). Argon ion bombardment on highly-oriented pyrolytic graphite (HOPG) was considered as a possible model to find the interactions between graphitic defects and the electronic structure. Finally, we used polycyclic aromatic hydrocarbons (PAHs) attached to graphene to observe structural and electrochemical changes associated with the architecture of carbon edge sites.

2. RESULTS AND DISCUSSION

Two activation procedures were used to compare felt electrodes that differed in their electrocatalytic activity and structural properties. First, a deoxygenation process using a mixture of argon and H_2 gas was employed to purify the surface of oxygen (GF- H_2).²⁶ Second, a thermally activated sample oxidized in air (GF-TA) was chosen to consider a conventional treatment relevant to the industrial scale. As the first step, the electrocatalytic activity for the vanadium oxidation was evaluated in electrochemical half-cell experiments. In this work, we focused on the $V^V O_2^+ / V^{IV} O^{2+}$ reaction as an example because it is kinetically sluggish and in general harder to facilitate. Furthermore, lots of contradicting results on the relationship between activity, surface chemistry, and structural properties exist, which makes resolving the relevant properties of the electronic structure more relevant. It should be mentioned that the relevant parameters obtained for the oxidation of vanadium species in the positive half-cell do not necessarily correspond to those driving reductive reactions in a VFB such as the V^{III} / V^{II} reduction reaction in the negative half-cell.

To describe the activity of an electrode, the peak potential separation (ΔE) can be determined by cyclic voltammetry (CV) and the charge transfer resistance (R_{CT}) by electrochemical impedance spectroscopy (EIS). It was found that the ΔE decreased from 230 (GF) to 140 (GF- H_2) to 100 mV (GF-TA) after activation (Figure 2a). Correspondingly, the R_{CT} decreased from 22 to 3 to 1 Ω in the same order (Figure 2b). This demonstrated that both activation methods increased

the electrocatalytic activity of GF but thermal oxidation did so to a greater extent.

To explain the differences in electrocatalytic activity, the physicochemical properties of the felts were studied. Structural defects and morphological changes on the microscale resulting from the treatments were visualized by SEM. Figure 2c–e shows that the smooth surface of the GF was preserved after deoxygenation, but additional pores were created by thermal activation. While the total surface area of GF-TA ($3.41 \text{ m}^2 \text{ g}^{-1}$) is larger than those of the GF ($0.64 \text{ m}^2 \text{ g}^{-1}$) and GF- H_2 ($0.69 \text{ m}^2 \text{ g}^{-1}$), it should be noted that in a previous study, we found that the active surface area normalized to the electrochemical double layer is higher for the latter due to a higher density of defects.²⁶

A deeper investigation down to the nanoscale was achieved by Raman spectroscopy (Figure 2f–h). The additional presence of defects on GF- H_2 was detected by evaluating the intensity ratio of the D and G bands in the spectra.²⁷ The graphite-related G-band at $\sim 1560 \text{ cm}^{-1}$ results from the in-plane stretching of C=C bonds, while the disorder-induced D-band at $\sim 1330 \text{ cm}^{-1}$ occurs from the breathing of C_6 rings.^{28,29} The $I(D)/I(G)$ ratio increased from 2.00 (GF) to 2.25 (GF- H_2) to 2.65 (GF-TA), indicating that both activation methods introduced additional defects, but thermal activation yielded more disorder. In addition, the half-width of the D-band increased from 49 to 57 cm^{-1} for GF-TA, which can be attributed to the increased number of defects.

The chemical composition studied by XPS showed surfaces consisting of carbon and oxygen only (Figure S1). No oxygen was present on GF- H_2 due to the deoxygenation process. The oxygen concentration decreased after thermal oxidation from 6.0 at % on the GF to 4.5 at % on GF-TA, which can be attributed to the removal of the atmospherically oxidized upper graphite layer, exposing an underlying, less oxidized layer. This is consistent with our previous study on surface oxygenation of GF, which showed that surface oxygen has a detrimental effect, if any, on catalytic activity. To quantitatively describe the degree of graphitization of a carbonaceous sample, the D-

parameter, evaluated in the first-derivative of the C KLL Auger region, can be used. It shows values of ~ 13 eV for diamond (sp^3) and up to 24 eV for graphite (sp^2).³⁰ In our case, the D-parameter of GF (22 eV) was increased after deoxygenation (23 eV) and decreased for GF-TA (21 eV). Accordingly, deconvolution of the C 1s spectra revealed that the sp^2 content increased for GF- H_2 (81 to 88 at %) and decreased after thermal activation (to 79 at %). This agreed well with the disorder characterized above by SEM and Raman spectroscopy and demonstrates that the $I(D)/I(G)$ ratio is a reliable tool to understand the catalytic activity of the GF.

Another method to study the integrity of the graphite structure, especially the upper surface layers, is REELS. A beam of electrons with a certain energy are scattered on the surface of the sample. Most of the electrons are scattered elastically, but a small fraction transfers energy to the system by exciting internal energetic transitions. In graphitic materials such as HOPG, a well-defined $\pi-\pi^*$ transition can be observed at 6.6 eV (Figure S2). The relative intensity and position of the loss feature characterize the graphitic degree, as demonstrated by argon ion bombardment: The inelastic scattering feature weakened and shifted to lower energy loss values. A higher degree of graphitization for GF- H_2 was therefore indicated by REELS through the relative intensity of the $\pi-\pi^*$ transition, in contrast to the low-intensity signal for GF-TA (Figure 3a).³¹ However, both samples showed a slight shift from 6.1 eV (GF) to lower energy values of 6.0 (GF- H_2) and 5.9 (GF-TA) due to the damaging pretreatment.

To establish correlations between the previously evaluated characteristics and the electronic structure, UPS was used to study the density of states near the Fermi level. Compared to XPS, which permits the emission of electrons from the first 10 nm of a sample, UPS is much more surface-sensitive, penetrating only the first 2.5 nm due to the lower excitation energy. Consequently, the electronic structure of the surface can be evaluated with high resolution. For graphitic materials, the range from 2 to 12 eV below E_F is occupied by C 2p electrons and >12 eV by C 2s electrons (Figure 3b).^{32,33} The region of the C 2p orbital can be divided into two contributions originating from $2p-\pi$ and $2p-\sigma$ electrons. The density of states extends until E_F where the π and π^* bands touch, characterizing graphite as a zero band-gap semiconductor.³⁴ For GF- H_2 , a strong $2s-\sigma$ signal at ~ 13 eV was detected due to the higher graphitic degree of the sample.³⁵ In addition to differences in valence band occupation which describe the electronic structure of the material, an energy cutoff at higher binding energies can be used to determine the WF. This value can be accurately evaluated with a bias voltage applied to the specimen, increasing the slope of the cutoff (Figure 3c). In addition, an energy threshold near E_F was used to define the VBM of the respective atomic orbital to describe the energetic level at which the charge carriers are located (Figure 3d).

The values of the electronic structure were used to draw a schematic band diagram (Figure 3e), in which we define the Fermi level as the reference point for the comparison of the samples. Since we assume that underlying graphite layers, which were not affected by the treatment, resemble the surface of the untreated GF, we define an energetic passage between the different materials at E_F , as shown in the scheme. It is observed that the WF decreased from 4.6 eV for the GF through 4.4 eV for the more active GF- H_2 to 4.2 eV for GF-TA, which has the highest electrocatalytic activity. Moreover,

an inverse correlation between the WF and the degree of disorder characterized by Raman spectroscopy can be established: a lower WF corresponds to a higher $I(D)/I(G)$ ratio. The VBM of the $2p-\pi$ electrons slightly increased after deoxygenation (1.5 to 1.6 eV), which we also observed in a previous work.²⁶ In contrast, the values for GF-TA remain unchanged, indicating that the disorder introduced through deoxygenation and thermal activation does not have a large effect on the electronic structure in the valence band.

Charge accumulation was detected at the interface between the untreated felt and the deoxygenated surface by a shifted C 1s signal (+0.1 eV). In our drawing, this is sketched as a downward band bending behavior typically known from semiconductors. Since GF and GF- H_2 both exhibit the properties of a semiconductor and we have defined GF to resemble the bulk beneath the modified surface layers, two semiconducting materials touch at the interface between the surface and bulk. We attribute this bending to a lower electrical conductivity in the direction perpendicular to the surface, in which the graphene layers are arranged, due to their higher degree of graphitization. To confirm that differences in the electronic structure are mainly linked to structural disorder and not the concentration or presence of surface oxygen groups, the thermally activated felt (GF-TA) was subjected to the deoxygenation and analysis procedure (Figure S3). Only slight changes were observed for deoxygenated GF-TA. The treatment resulted in a further decrease of the WF and VBM to 4.1 eV and 1.6 eV, respectively. In agreement with our previous study on GF-TA, which showed that charge transfer properties can be enhanced by the removal of surface oxygen, this is further evidence that the WF and catalytic activity are linked.^{26,36}

To study the effects of disorder on the electronic structure in more detail, HOPG was chosen as a model substrate. Initially, the HOPG surface was contaminated by atmospheric oxidation and thus exhibited oxygen (~ 4 at %), a low D parameter (17 eV), and a reduced sp^2 carbon content of ~ 78 at % (Figure S4). In the second step, the surface was cleaned with argon ion clusters, which increased the D parameter to 24 eV and the sp^2 content to ~ 93 at %, as expected for an almost perfect graphitic material. Subsequently, defects were introduced by bombardment with monoatomic argon ions. This resulted in an additional contribution in the C 1s spectra due to the formation of carbon vacancies.³⁷ At all three stages of the substrate (untreated, cleaned, and etched), UPS was used to follow the evolution of the electronic structure and sketch a band diagram (Figures S2 and S5). Removal of oxygen and sp^3 carbon resulted in a sharp drop in the WF from 4.9 to 4.2 eV. However, this value was maintained after ion bombardment, which illustrates that vacancies do not affect the level of the WF. Instead, the VBM of the $2p-\pi$ electrons increased from 0.9 to 0 eV, indicating a metallic character for the damaged HOPG. This highlights the different influences of various defects on the electronic properties of graphite. Point defects introduced by ion bombardment altered the VBM similar to the introduction of additional charge carriers by doping. Argon ions implanted in the material during ion bombardment cannot be held responsible for the changes in the electronic structure since at the time of the UPS measurements, the volatile argon has already escaped through the defects into the atmosphere. This is confirmed by the absence of argon-related signals in the spectra after bombardment. The presence of predominant edge defects on the GF is evident from previous

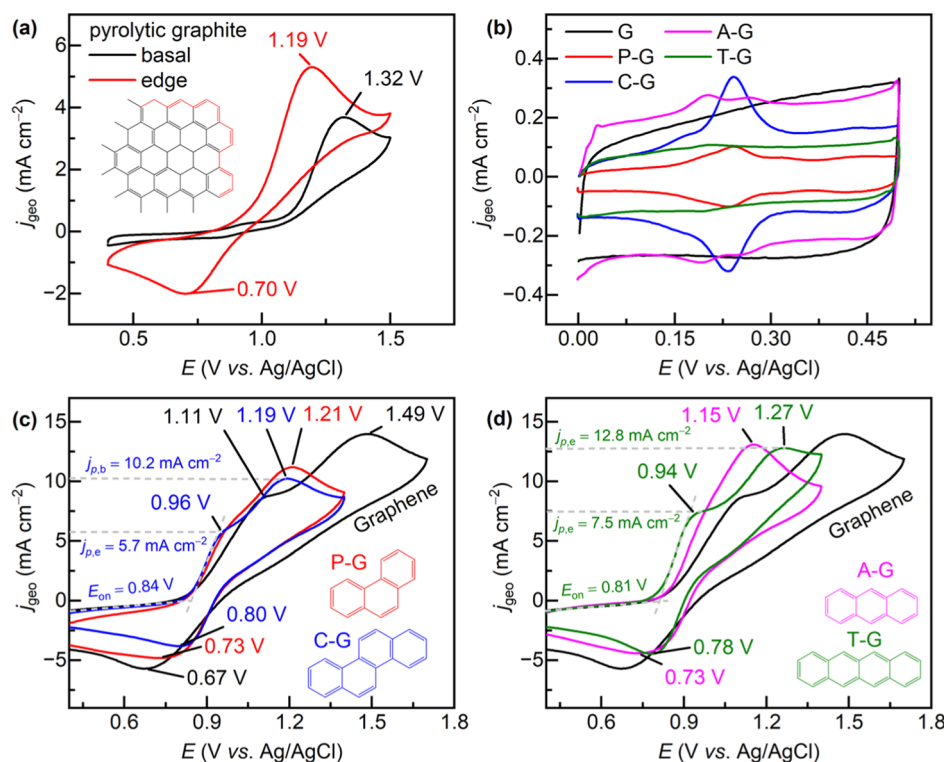


Figure 4. Electrochemical characterization of carbon edge sites in the 0.1 M $V^{IV}O_2^+/2$ M H_2SO_4 electrolyte. (a) Comparison of the basal and edge plane of pyrolytic graphite; (b) current response in the double-layer region, and (c,d) electrocatalytic activity of (c) armchair and (d) zigzag-edge site PAH-modified graphene.

studies in which we investigated the nature of disorder by Raman spectroscopy and from the absence of an additional peak in the C 1s spectra after the activation (Figure S1) that would correspond to vacancies.^{26,36} The edge sites on GF- H_2 and GF-TA, on the other hand, decrease the WF but leave the valence band level unchanged.

The importance of edge sites for the electrocatalysis of vanadium redox reactions is demonstrated by the CV curves of pyrolytic graphite electrodes exposing either predominately basal or edge planes (Figure 4a). For the HOPG electrode with the edge site orientation, the $V^{IV}O_2^+/V^{IV}O_2^+$ oxidation wave exhibited higher peak currents and was shifted to lower potentials, confirming the higher reactivity of these regions compared to the basal plane. However, since edge sites have both armchair and zigzag configuration in real electrodes, their individual contribution cannot be assessed by this measurement. Therefore, we modified graphene with PAHs that differ in their orientation and number of conjugated rings. We chose two PAHs with armchairs, phenanthrene (P-G) and chrysene (C-G), and two with zigzag edges, anthracene (A-G) and tetracene (T-G), with three and four rings, respectively, to account for the edge type and size effect. The successful modification was observed by redox signals in a potential region where graphene otherwise shows no Faradaic current response (Figure 4b).

The modified graphene powders were then used to evaluate their electrocatalytic activity (Figure 4c,d). In the CV curves, pure graphene shows two oxidation peaks. We assume that these signals do either correspond to the basal plane (1.49 V) and the more active edges (1.11 V) of its finite platelets similar to the observations on pyrolytic graphite, or they arise due to two edge-related carbon atoms: There could be an electrochemical difference between sp²- and sp³-bound carbon at the

edge of one C₆ ring and between two conjugated rings. The electrocatalytic activity increased for all PAH-modified electrodes, evidenced by a shift of both oxidation signals to lower potentials. However, differences were observed for the onset and peak potential of the oxidation, as well as in the maximum peak current. A larger π -conjugated system in the form of four conjugated rings shows a more defined first signal (C-G and T-G), while for the three-ring PAHs, the two peaks almost merge. Comparing the armchair (C-G) to zigzag edges (T-G) with four rings, the onset potential decreases from 0.84 to 0.81 V, the first peak potential increases from 0.96 to 1.94 V, and its peak current increases from 5.7 to 7.5 mA cm⁻². These results highlight two important findings: first, the role of edge geometry, with zigzag edges being superior to armchair edges, and second, the importance of π -conjugation, showing that larger graphitic systems can use their edges more effectively.

We then investigated the structural and electronic properties of the modified powders to find a descriptor for the differences in activity. Raman spectroscopy revealed no discernible differences between the samples (Figure S6), which can be attributed to the strong signal contribution of the underlying graphene. In contrast, due to the high surface sensitivity of REELS and UPS, the changes in the electronic properties could be well observed. To establish meaningful correlations, the least and most reactive PAHs, P-G and T-G, were analyzed in detail and compared with the original graphene. We first made sure that the chemical composition of the surface remained almost unchanged after modification. Only T-G showed a slight increase in the oxygen content, which can be attributed to the higher chemical reactivity of the zigzag edges (Figure S7).³⁸ However, as demonstrated, even the surface oxygen contents of >4 at % did not significantly affect the results of the electronic structure analysis. As for GF- H_2 ,

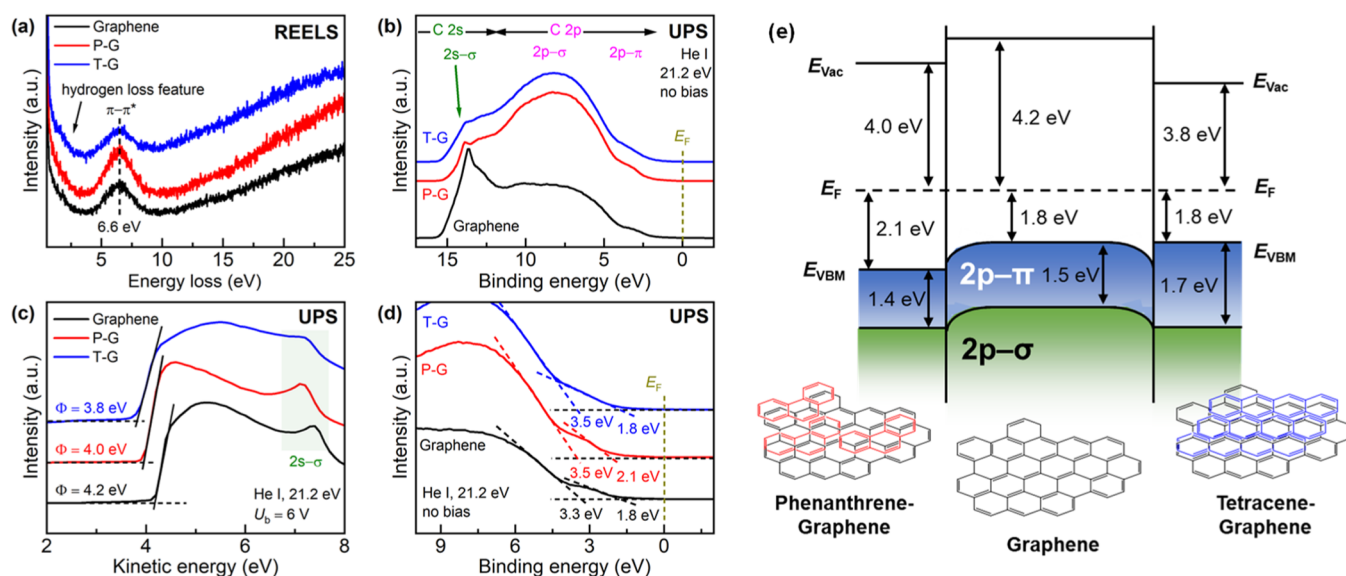


Figure 5. Electronic structure of natural vs armchair vs zigzag carbon edge sites. (a) π – π^* transition in REELS; (b) electronic density below E_F , probed by UPS. (c) At an applied external bias, the cutoff energy of the valence electrons yields the WF. (d) Detailed investigation of the threshold energies close to E_F . (e) Model of the electronic band diagram.

charge accumulation at the interface between graphene and PAH is evidenced by a slight shift in the sp^2 carbon peak in the C 1s spectra (+0.2 eV), which could be attributed to the electrically insulating property of the PAH. The π – π^* transition recorded by REELS was more pronounced in P-G because a layer of fully π -conjugated electrons has been added by the armchair ribbons (Figure 5a). In contrast, the transition peak of T-G decreased due to the perturbation of the system, forming π -radicals responsible for the higher chemical reactivity of the zigzag edges.³⁹

Graphene showed a strong contribution of $2s$ – σ electrons in the UPS spectra, which was drastically reduced after modification with nongraphitic PAH (Figure 5b). Again, the WF and VBM were extracted from the UPS spectra by careful examination of the cutoff energy at applied bias and the region near the Fermi level (Figure 5c,d). In the band diagram in Figure 5e, it is seen that the WF of graphene is the same as that of cleaned HOPG (4.2 eV), but it is significantly reduced by the attached PAHs. Charge accumulation at the interface of graphene and PAH was again sketched as band bending behavior. Armchair edges have a semiconducting, and zigzag edges have a metallic character.⁴⁰ This explains why the VBM reduced for P-G (from 1.8 to 2.1 eV); however, it did not further increase for T-G.^{40–42} Again, the electrocatalytic activity of the materials corresponds well to their respective WF levels, reconfirming the importance of this parameter previously derived from the analysis of the modified GF electrodes. The WF is reduced by the additional armchair edges of the P-G (4.0 eV) but even more by the zigzag edges of the highly active T-G (3.8 eV). In summary, our results show a clear correlation between the electronic structure, microstructure, and electrocatalytic activity and prove that the decrease of the work function, which can be achieved by the introduction of (preferably zigzag) edge sites, effectively increases the electrocatalytic activity of graphite.

3. CONCLUSIONS

Pristine, thermally activated, and deoxygenated GF electrodes were studied to investigate the correlation between catalytic

activity and structural and electronic properties. Morphological defects, such as edge sites, form the basis for successful charge transfer in the vanadium oxidation occurring in flow batteries. These defects were investigated by Raman spectroscopy and SEM to establish a correlation between the catalytic activity and the microstructure. By examining the electronic structure using UPS, we found that the catalytic activity correlates with the WF level of the material. Argon bombardment of HOPG showed that point defects do not affect the WF but instead increase the electron density near the Fermi level. PAHs exhibiting armchair and zigzag edges were used to investigate the importance of edge site configuration in catalytic activity and the electronic structure. The zigzag edges, which required the lowest overvoltage and provided the highest current densities for the oxidation of $V^{IV}O_2^{2+}$ to $V^{V}O_2^+$, also showed the lowest WF. These results clearly demonstrate the dependencies between structural, electronic, and electrochemical properties. Conflicting results in the literature on the role of surface chemistry for carbon-based electrodes could be addressed in the future by additional investigation of the electronic structure.

4. EXPERIMENTAL SECTION

4.1. Sample Preparation. Sheets of pristine PAN-based and thermally activated GF (SGL Carbon, GFD 4.6) were cut and cleaned by sonication in isopropanol and ultrapure Milli-Q water ($18.2 \text{ M}\Omega \text{ cm}^{-1}$) for 10 min each, followed by drying at 80 °C. For deoxygenation, a previously proposed method was used.²⁶ The felts were heated in a gas-tight sealed quartz glass tube at 980 °C for 3 h under argon. After cooling, a hydrogen gas flow saturates dangling bonds and prevents oxidation.

Defect-free graphene (Dasheng Co. Ltd., China) was used as a substrate to prepare model catalysts with armchair and zigzag edge sites. PAHs phenanthrene, anthracene, chrysene, and tetracene (all with a purity $\geq 99\%$) were obtained from Sigma-Aldrich and used according to the literature.²⁵ PAHs and graphene were dispersed in dimethyl sulfoxide (DMSO) under ultrasound and stirred overnight. The product was filtered, washed with Milli-Q several times to remove excess PAHs and

DMSO, and dried at 80 °C. To form a dispersion for electrochemical measurements, 4 mg of the product was dispersed in a mixture of 390 μL of isopropanol and 10 μL of Nafion solution (5 wt %, Sigma-Aldrich).

4.2. X-ray and Electron Spectroscopy. XPS, UPS, and REELS were performed using an ESCALAB 250Xi spectrometer (Thermo Fisher Scientific). The integrity of the spectrometer was confirmed by measuring fresh argon-sputtered gold as the reference. The Au $4f_{7/2}$ transition at 84.0 eV and the Fermi level located at 0 eV were used for calibration. Furthermore, the WF ($\varphi = 5.1 \pm 0.1$ eV) was verified at each applied bias.

For XPS, monochromatic Al-K α radiation ($E = 1486.6$ eV) at a spot size of ~ 650 μm was used. Survey spectra were recorded with a pass energy of 200 eV and high-resolution spectra with 50 eV. Two spots were measured on every sample to rule out deviation. The Avantage software was used for data acquisition and spectra deconvolution, applying Shirley background correction by the implemented smart background function. Single species were deconvoluted by Voigt profiles. The asymmetry of sp^2 -hybridized carbon was assessed with a tail mix of 80 to 90% and a tail exponent of 0.03 to 0.4. The position of the residual components in the C 1s region was restricted to the position of sp^2 carbon and the full width at half-maximum (fwhm) values to the sp^3 carbon signal with a tolerance of ± 0.1 eV. The O 1s region was deconvoluted by multiple peaks with 1 ± 0.1 eV distance, restricting the fwhm by ± 0.1 eV for all oxygen groups. For the investigation of the D-parameter, the C KLL Auger region was scanned 100 times with a pass energy of 100 eV and a step size of 0.5 eV. The D-parameter was then determined by the distance between the intensity maximum and minimum in a first-derivative plot. The samples were treated inside the UHV by argon ion bombardment. Mild surface cleaning was achieved by argon clusters consisting of 300 atoms with an energy of 4 keV (~ 13 eV/atom) for 60 s. Ion etching was conducted by monoatomic sputtering at 3 keV for 60 s.

For UPS, a helium gas discharge lamp ($E = 21.22$ eV) was used to generate photoelectrons in the valence band with high resolution. The spectra were recorded with a pass energy of 2 eV and a step size of 0.1 eV. To determine the WF, a bias voltage of 4 to 6 V was applied. By fitting the threshold close to E_F and the cutoff energy, the valence band maxima and the WF were determined, respectively.

REELS was carried out at an electron source energy of 1 keV, scanning the elastic and the inelastic peaks with a pass energy of 5 and 10 eV, respectively, at a step size of 0.02 eV. To compare the pattern of multiple samples, the inelastic signals were normalized to the intensity of the corresponding elastic.

4.3. Raman Spectroscopy. The degree of disorder was investigated by Raman spectroscopy, using a LabRAM HR Evolution spectrometer (HORIBA scientific), equipped with a HeNe laser ($\lambda = 632.8$ nm, $E = 1.9876$ eV). A 600 grooves mm^{-1} grating along with a 50 \times magnification objective was employed. On each sample, at least five spectra were averaged. The CasaXPS software was used to apply a cubic spline background and for spectra deconvolution. Absolute Lorentzian peak shapes were used for the D, G, and D' band and mixed Gaussian–Lorentzian for the residual features.

4.4. Scanning Electron Microscopy. The morphology of the samples was investigated by field emission scanning

electron microscopy (FE-SEM, Merlin, Carl Zeiss) at an acceleration voltage of 5 kV and a probe current of 250 pA.

4.5. Electrochemistry. As the electrolyte, 0.1 M $V^{IV}O^{2+}$ was prepared by dissolving $VOSO_4$ powder (Alfa Aesar) in 2 M H_2SO_4 (Emsure). The electrocatalytic activity of the GF was studied by CV and EIS in a custom-built three-electrode cell connected to a potentiostat (VSP, BioLogic). Another GF of at least 5 times the size was used as the counter electrode, and Ag/AgCl stored in 3 M KCl ($E_{Ag/AgCl} = 0.210$ V vs the reversible hydrogen electrode) as the reference electrode. Prior to the experiments, the samples were centrifuged in the electrolyte for 5 min at 800 rpm.

10 μL of the model catalyst dispersion was drop-coated on PEEK-encased glassy carbon (ALS) and measured in a glass vessel using the same reference specified above and a graphite rod (redox.me) as the counter electrode. Prior to the coating, the glassy carbon was polished on a cloth using an aluminum suspension (Buehler, 0.5 μm) before being ultrasonically cleaned in isopropanol and Milli-Q. Basal and edge plane-exposed PEEK-encased pyrolytic graphite electrodes (ALS) were further used. To ensure a fresh basal plane, the upper layers were removed using conventional tape. The edge plane was prepared by polishing.

Electrolyte-filled cells were freed from gas with argon. An electrochemical surface conditioning step was performed to remove loose surface adsorbates by scanning 20 times from 0 to 0.5 V vs Ag/AgCl with 100 mV s^{-1} . CV measurements were conducted at a scan rate of 1 mV s^{-1} for the GF and 10 mV s^{-1} for the model catalyst. The data of the GF was iR -corrected according to the resistance of the electrolyte by performing EIS at the open-circuit potential (Figure S8). Impedance spectra at an applied potential (0.9 V vs Ag/AgCl) were recorded with a voltage amplitude of 10 mV to assess the charge-transfer resistance (R_{CT}). Spectra were evaluated by the RelaxIS 3 software (rhd instruments), using the equivalent circuit diagram displayed in Figure 2b. Two semicircles can be seen in the impedance spectra, the small first one corresponding to the interface between GF and the glassy carbon current collector and the large second one corresponding to the interface between the GF and the electrolyte, that is, the charge transfer.

■ ASSOCIATED CONTENT

Supporting Information

The Supporting Information is available free of charge at <https://pubs.acs.org/doi/10.1021/acscatal.2c00334>.

XPS and EIS of pristine and activated GF; XPS, UPS, REELS, and band diagram of the pristine, Ar-cleaned, and Ar-etched HOPG; UPS and REELS of deoxygenated GF-TA; and Raman spectra and XPS of PAH-modified graphene (PDF)

■ AUTHOR INFORMATION

Corresponding Author

Hannes Radinger – Institute for Applied Materials, Karlsruhe Institute of Technology, Eggenstein-Leopoldshafen 76344, Germany; orcid.org/0000-0001-5087-0272; Email: hannes.radinger@kit.edu

Authors

Vanessa Trouillet – Institute for Applied Materials, Karlsruhe Institute of Technology, Eggenstein-Leopoldshafen 76344, Germany

Felix Bauer – Institute for Applied Materials, Karlsruhe Institute of Technology, Eggenstein-Leopoldshafen 76344, Germany

Frieder Scheiba – Institute for Applied Materials, Karlsruhe Institute of Technology, Eggenstein-Leopoldshafen 76344, Germany; orcid.org/0000-0001-7275-3077

Complete contact information is available at:
<https://pubs.acs.org/10.1021/acscatal.2c00334>

Notes

The authors declare no competing financial interest.

ACKNOWLEDGMENTS

The financial support by the German Federal Ministry of Education and Research within the project Flow3DKat (03EK3053C) is gratefully acknowledged. This work contributes to the research performed at the Center for Electrochemical Energy Storage Ulm-Karlsruhe (CELEST). H.R. acknowledges the access to the surface science equipment by the Karlsruhe Nano Micro Facility (KNMF).

REFERENCES

- (1) Togonon, J. J. H.; Chiang, P.-C.; Lin, H.-J.; Tsai, W.-C.; Yen, H.-J. Pure carbon-based electrodes for metal-ion batteries. *Carbon Trends* **2021**, *3*, 100035.
- (2) Zhang, L. L.; Zhao, X. S. Carbon-based materials as supercapacitor electrodes. *Chem. Soc. Rev.* **2009**, *38*, 2520–2531 Published Online: Jun. 12, 2009.
- (3) Li, S.; Cheng, C.; Thomas, A. Carbon-Based Microbial-Fuel-Cell Electrodes: From Conductive Supports to Active Catalysts. *Adv. Mater.* **2017**, *29*, 1602547 Published Online: Dec. 19 2016.
- (4) Zhang, G.; Cuharuc, A. S.; Güell, A. G.; Unwin, P. R. Electrochemistry at highly oriented pyrolytic graphite (HOPG): lower limit for the kinetics of outer-sphere redox processes and general implications for electron transfer models. *Phys. Chem. Chem. Phys.* **2015**, *17*, 11827–11838.
- (5) Pour, N.; Kwabi, D. G.; Carney, T.; Darling, R. M.; Perry, M. L.; Shao-Horn, Y. Influence of Edge- and Basal-Plane Sites on the Vanadium Redox Kinetics for Flow Batteries. *J. Phys. Chem. C* **2015**, *119*, 5311–5318.
- (6) Park, M.; Jeon, I.-Y.; Ryu, J.; Baek, J.-B.; Cho, J. Exploration of the Effective Location of Surface Oxygen Defects in Graphene-Based Electrocatalysts for All-Vanadium Redox-Flow Batteries. *Adv. Energy Mater.* **2015**, *5*, 1401550.
- (7) Taylor, S. M.; Pătru, A.; Perego, D.; Fabbri, E.; Schmidt, T. J. Influence of Carbon Material Properties on Activity and Stability of the Negative Electrode in Vanadium Redox Flow Batteries: A Model Electrode Study. *ACS Appl. Energy Mater.* **2018**, *1*, 1166–1174.
- (8) Sun, B.; Skyllas-Kazacos, M. Modification of graphite electrode materials for vanadium redox flow battery application—I. Thermal treatment. *Electrochim. Acta* **1992**, *37*, 1253–1260.
- (9) Sun, B.; Skyllas-Kazacos, M. Chemical modification of graphite electrode materials for vanadium redox flow battery application—part II. Acid treatments. *Electrochim. Acta* **1992**, *37*, 2459–2465.
- (10) Radinger, H. A surface odyssey. The role of oxygen functional groups on activated carbon-based electrodes in vanadium flow batteries. *ChemPhysChem* **2021**, *22*, 2498–2505.
- (11) Wei, G.; Su, W.; Wei, Z.; Fan, X.; Liu, J.; Yan, C. Electrocatalytic effect of the edge planes sites at graphite electrode on the vanadium redox couples. *Electrochim. Acta* **2016**, *204*, 263–269.
- (12) Yuan, W.; Zhou, Y.; Li, Y.; Li, C.; Peng, H.; Zhang, J.; Liu, Z.; Dai, L.; Shi, G. The edge- and basal-plane-specific electrochemistry of a single-layer graphene sheet. *Sci. Rep.* **2013**, *3*, 2248.
- (13) Boukhalov, D. W.; Katsnelson, M. I. Chemical Functionalization of Graphene with Defects. *Nano Lett.* **2008**, *8*, 4373–4379.
- (14) Hassan, A.; Haile, A. S.; Tzedakis, T.; Hansen, H. A.; Silva, P. de. The Role of Oxygenic Groups and sp³ Carbon Hybridization in Activated Graphite Electrodes for Vanadium Redox Flow Batteries. *ChemSusChem* **2021**, *14*, 3945–3952 Published Online: Jul. 29, 2021.
- (15) Luque, N. B.; Schmickler, W. The electric double layer on graphite. *Electrochim. Acta* **2012**, *71*, 82–85.
- (16) Wei, D.; Liu, Y.; Wang, Y.; Zhang, H.; Huang, L.; Yu, G. Synthesis of N-doped graphene by chemical vapor deposition and its electrical properties. *Nano Lett.* **2009**, *9*, 1752–1758.
- (17) Luo, Z.; Lim, S.; Tian, Z.; Shang, J.; Lai, L.; MacDonald, B.; Fu, C.; Shen, Z.; Yu, T.; Lin, J. Pyridinic N doped graphene: synthesis, electronic structure, and electrocatalytic property. *J. Mater. Chem.* **2011**, *21*, 8038.
- (18) Radinger, H.; Hartmann, M.; Ast, M.; Pfisterer, J.; Bron, M.; Ehrenberg, H.; Scheiba, F. Understanding Efficient Phosphorus-Functionalization of Graphite for Vanadium Flow Batteries. *Electrochim. Acta*, **2022**, 139971. DOI: [10.1016/j.electacta.2022.139971](https://doi.org/10.1016/j.electacta.2022.139971).
- (19) Vayenas, C. G.; Bebelis, S.; Ladas, S. Dependence of catalytic rates on catalyst work function. *Nature* **1990**, *343*, 625–627.
- (20) Ismail, A. M.; Csapó, E.; Janáky, C. Correlation between the work function of Au–Ag nanoalloys and their electrocatalytic activity in carbon dioxide reduction. *Electrochim. Acta* **2019**, *313*, 171–178.
- (21) Liu, T.; Xi, C.; Dong, C.; Cheng, C.; Qin, J.; Hu, S.; Liu, H.; Du, X.-W. Improving Interfacial Electron Transfer via Tuning Work Function of Electrodes for Electrocatalysis: From Theory to Experiment. *J. Phys. Chem. C* **2019**, *123*, 28319–28326.
- (22) Cai, Y.; Tao, L.; Huang, G.; Zhang, N.; Zou, Y.; Wang, S. Regulating carbon work function to boost electrocatalytic activity for the oxygen reduction reaction. *Chin. J. Catal.* **2021**, *42*, 938–944.
- (23) Choi, C. H.; Lim, H.-K.; Chung, M. W.; Chon, G.; Ranjbar Sahraie, N.; Altin, A.; Sougrati, M.-T.; Stievano, L.; Oh, H. S.; Park, E. S.; Luo, F.; Strasser, P.; Dražić, G.; Mayrhofer, K. J. J.; Kim, H.; Jaouen, F. The Achilles' heel of iron-based catalysts during oxygen reduction in an acidic medium. *Energy Environ. Sci.* **2018**, *11*, 3176–3182.
- (24) Ritter, K. A.; Lyding, J. W. The influence of edge structure on the electronic properties of graphene quantum dots and nanoribbons. *Nat. Mater.* **2009**, *8*, 235–242 Published Online: Feb. 15, 2009.
- (25) Lin, Y.; Lu, Q.; Song, F.; Yu, L.; Mechler, A. K.; Schlögl, R.; Heumann, S. Oxygen Evolution Reaction at Carbon Edge Sites: Investigation of Activity Evolution and Structure-Function Relationships with Polycyclic Aromatic Hydrocarbons. *Angew. Chem., Int. Ed.* **2019**, *58*, 8917–8921 Published Online: May. 17, 2019.
- (26) Radinger, H.; Ghamlouche, A.; Ehrenberg, H.; Scheiba, F. Origin of the catalytic activity at graphite electrodes in vanadium flow batteries. *J. Mater. Chem. A* **2021**, *9*, 18280–18293.
- (27) Ammar, M. R.; Galy, N.; Rouzaud, J. N.; Toulhoat, N.; Vaudey, C. E.; Simon, P.; Moncoffre, N. Characterizing various types of defects in nuclear graphite using Raman scattering: Heat treatment, ion irradiation and polishing. *Carbon* **2015**, *95*, 364–373.
- (28) Tuinstra, F.; Koenig, J. L. Raman Spectrum of Graphite. *J. Chem. Phys.* **1970**, *53*, 1126–1130.
- (29) Sato, K.; Saito, R.; Oyama, Y.; Jiang, J.; Cañado, L. G.; Pimenta, M. A.; Jorio, A.; Samsonidze, G.; Dresselhaus, G.; Dresselhaus, M. S. D-band Raman intensity of graphitic materials as a function of laser energy and crystallite size. *Chem. Phys. Lett.* **2006**, *427*, 117–121.
- (30) Lesiak, B.; Kövér, L.; Tóth, J.; Zemek, J.; Jiricek, P.; Kromka, A.; Rangam, N. C. sp²/sp³ hybridisations in carbon nanomaterials – XPS and (X)AES study. *Appl. Surf. Sci.* **2018**, *452*, 223–231.
- (31) Werner, W. S.; Bellissimo, A.; Leber, R.; Ashraf, A.; Segui, S. Reflection electron energy loss spectrum of single layer graphene measured on a graphite substrate. *Surf. Sci.* **2015**, *635*, L1–L3.

(32) Ganguly, A.; Sharma, S.; Papakonstantinou, P.; Hamilton, J. Probing the Thermal Deoxygenation of Graphene Oxide Using High-Resolution In Situ X-ray-Based Spectroscopies. *J. Phys. Chem. C* **2011**, *115*, 17009–17019.

(33) McFeely, F. R.; Kowalczyk, S. P.; Ley, L.; Cavell, R. G.; Pollak, R. A.; Shirley, D. A. X-ray photoemission studies of diamond, graphite, and glassy carbon valence bands. *Phys. Rev. B* **1974**, *9*, 5268–5278.

(34) Rabchinskii, M. K.; Ryzhkov, S. A.; Kirilenko, D. A.; Ulin, N. V.; Baidakova, M. V.; Shnitov, V. V.; Pavlov, S. I.; Chumakov, R. G.; Stolyarova, D. Y.; Besedina, N. A.; Shvidchenko, A. V.; Potorochin, D. V.; Roth, F.; Smirnov, D. A.; Gudkov, M. V.; Brzhezinskaya, M.; Lebedev, O. I.; Melnikov, V. P.; Brunkov, P. N. From graphene oxide towards aminated graphene: facile synthesis, its structure and electronic properties. *Sci. Rep.* **2020**, *10*, 6902.

(35) Endo, K.; Koizumi, S.; Otsuka, T.; Ida, T.; Morohashi, T.; Onoe, J.; Nakao, A.; Kurmaev, E. Z.; Moewes, A.; Chong, D. P. Analysis of Electron Spectra of Carbon Allotropes (Diamond, Graphite, Fullerene) by Density Functional Theory Calculations Using the Model Molecules. *J. Phys. Chem. A* **2003**, *107*, 9403–9408.

(36) Radinger, H.; Pfisterer, J.; Scheiba, F.; Ehrenberg, H. Influence and Electrochemical Stability of Oxygen Groups and Edge Sites in Vanadium Redox Reactions. *ChemElectroChem* **2020**, *7*, 4745–4754.

(37) Ganesan, K.; Ghosh, S.; Gopala Krishna, N.; Ilango, S.; Kamruddin, M.; Tyagi, A. K. A comparative study on defect estimation using XPS and Raman spectroscopy in few layer nanographitic structures. *Phys. Chem. Chem. Phys.* **2016**, *18*, 22160–22167.

(38) Fujii, S.; Ziatdinov, M.; Ohtsuka, M.; Kusakabe, K.; Kiguchi, M.; Enoki, T. Role of edge geometry and chemistry in the electronic properties of graphene nanostructures. *Faraday Discuss.* **2014**, *173*, 173–199.

(39) Fujii, S.; Enoki, T. Nanographene and graphene edges: electronic structure and nanofabrication. *Acc. Chem. Res.* **2013**, *46*, 2202–2210.

(40) Son, Y.-W.; Cohen, M. L.; Louie, S. G. Energy gaps in graphene nanoribbons. *Phys. Rev. Lett.* **2006**, *97*, 216803 Published Online: Nov. 22, 2006.

(41) Barone, V.; Hod, O.; Scuseria, G. E. Electronic structure and stability of semiconducting graphene nanoribbons. *Nano Lett.* **2006**, *6*, 2748–2754.

(42) Nakada, K.; Fujita, M.; Dresselhaus, M. S. Edge state in graphene ribbons: Nanometer size effect and edge shape dependence. *Phys. Rev. B: Condens. Matter Mater. Phys.* **1996**, *54*, 17954–17961.

Recommended by ACS

Composition of Oxygen Functional Groups on Graphite Surfaces

Nadia N. Intan and Jim Pfaendtner

JUNE 23, 2022
THE JOURNAL OF PHYSICAL CHEMISTRY C

READ 

Cation Overcrowding Effect on the Oxygen Evolution Reaction

Jun Huang, Axel Groß, *et al.*

SEPTEMBER 30, 2021
JACS AU

READ 

Electrochemistry of Multilayer Electrodes: From the Basics to Energy Applications

Minsu Gu and Byeong-Su Kim

NOVEMBER 10, 2020
ACCOUNTS OF CHEMICAL RESEARCH

READ 

Cation-Dependent Multielectron Kinetics of Metal Oxide Splitting

Jaclyn R. Lunger, Yang Shao-Horn, *et al.*

APRIL 08, 2022
CHEMISTRY OF MATERIALS

READ 

Get More Suggestions >